

Rotor Displacement Control of Bearingless Switched Reluctance Motor with Single-Winding Stator

WANG Chuanchuan¹, ZHANG Junhao¹, JIN Lu²,
NIU Zhaoxiang¹, DU Juncheng¹, WANG Huijun^{1*}

1. School of Instrumentation and Optoelectronics Engineering, Beihang University, Beijing 100191, P.R. China;

2. Zhejiang Xizi Forvorda Electrical Machinery Co. Ltd., Hangzhou 311300, P.R. China

(Received 15 June 2023; revised 10 October 2023; accepted 21 January 2024)

Abstract: Rotor displacement control of a bearingless switched reluctance motor (BLSRM) with single-winding stator is proposed. First, the structure and working principle of BLSRM are briefly introduced. The equivalent magnetic circuit method is used to establish a mathematical model of suspension force and stiffness. In addition, a rotor-dynamic model is established to attain the relation between force and rotor displacement. Finally, a prototype motor is designed and the suspension control of the motor is implemented. The validity of the proposed method is verified by experimental results.

Key words: bearingless switched reluctance motor (BLSRM); rotor displacement; single-winding stator; control

CLC number: TN925

Document code: A

Article ID: 1005-1120(2024)03-0289-11

0 Introduction

Bearingless switched reluctance motor (BLSRM) combines advantages of SRM and magnetic bearing^[1-3]. It means motor not only supplies rotating torque but also provides levitation force. They are essentially free of maintenance and particularly suitable to operate in special environments such as blood pumps^[4-5].

Recently, several structures of BLSRM have been proposed, such as 12/8 double-winding structure^[6], 12/8 common-suspended double-winding structure^[7], 12/8 single-winding structure^[8], 8/6 single-winding structure^[9], 6/4 single-winding structure^[10] and 12/4 single-winding structure^[11-12]. According to the published papers, one common problem in these existing structures is that torque and suspension force are nonlinear functions of current and rotor position. At the same time, two magnetic fluxes, torque flux and suspending flux, cause a very strong coupling in the stator yoke and other

parts of the common magnetic circuit, which is very difficult to control and decouple. In addition, in order to generate a large suspension force, turn-on and turn-off angles for control torque have to be selected near the maximum position of the inductor, resulting in low utilization of the positive torque region. Moreover, torque current is not easy to be turned off at the large inductance and enters into the negative torque region, leading to a further reduction in the average torque.

In order to solve the coupling problem, one hybrid stator pole structure has been proposed, such as 8/10 structure^[13], 12/14 structure^[14-15], 12/12 axial permanent magnet structure^[16] and 12/14 axial permanent magnet structure^[17]. In these structures, torque pole on the stator generates torque while radial force pole generates suspending force. Since the BLSRM combines the motor with magnetic bearings, suspension performance is very important^[18-20]. In most cases, the suspension force is controlled at equilibrium position and the force is linear

*Corresponding author, E-mail address: huijunwang@buaa.edu.cn.

How to cite this article: WANG Chuanchuan, ZHANG Junhao, JIN Lu, et al. Rotor displacement control of bearingless switched reluctance motor with single-winding stator[J]. Transactions of Nanjing University of Aeronautics and Astronautics, 2024, 41(3):289-299.

<http://dx.doi.org/10.16356/j.1005-1120.2024.03.003>

ized to the sum of the product of current stiffness with current and displacement stiffness with displacement^[21]. Therefore, stiffness is very important for the design of the motor controller^[22].

In this paper, based on the proposed 12/14 single-winding BLSRM, one independent control scheme for levitation force is presented. First of all, the structure and working principle of the motor are briefly introduced. In the meanwhile, mathematical model is established to represent the suspension force and stiffness. Furthermore, a rotor-dynamic model is constructed. Based on the above analysis, the digital control system is designed and an experimental platform is established. Finally, experiments are carried out and motor can be steadily levitated in the static and rotating conditions.

1 Structure and Operation Principle

Fig.1 shows the three-dimensional structure of the motor, where the stator pole is composed of four suspension poles and eight torque poles. To obtain a continuous suspension force, the pole arc of the suspension pole is not smaller than one rotor pole pitch.

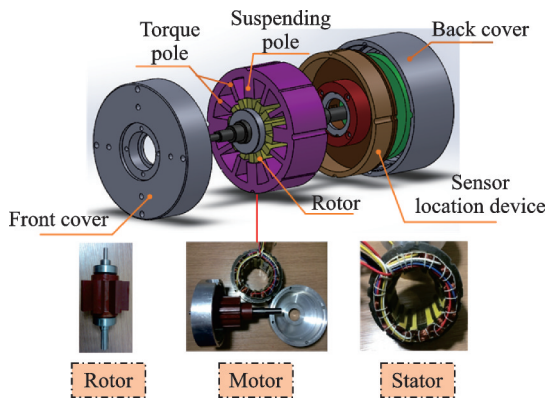


Fig.1 The proposed 12/14 structure

Fig.2 shows the connection of the torque winding and the suspension winding. It can be found that each stator pole only has one set of winding. The suspending poles have a pair of control windings, as shown with the blue line. And each pair of control coils control one degree of freedom in the radial

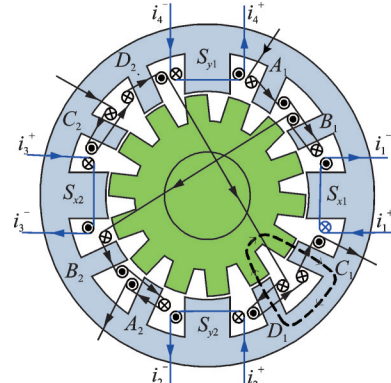


Fig.2 Winding connection

direction. In addition, there is a pair of torque winding coils for every four torque poles, where the magnetic flux of the torque flux has short path characteristic.

Since the rotor displacement has two degrees of freedom in the radial direction, four displacement sensors are installed on the motor to detect the rotor displacement, and every two sensors detect rotor eccentric displacement in one radial direction. For example, when the rotor moves in the Y^+ direction, the displacement sensor transmits the position signal to the controller, and the control current in the suspending windings on the poles S_{y1} and S_{y2} is transformed. As a result, the change in the total flux causes the rotor to move in the Y^- direction. By controlling the current in the winding coil, the rotor can be kept in the balance position.

2 Suspending Force

To calculate the suspension force of the proposed BLSRM, the equivalent magnetic circuit method is used, as shown in Fig.3. In addition, P_{x1} , P_{x2} , P_{y1} and P_{y2} are the permeances of air-gap under the suspending poles S_{x1} , S_{x2} , S_{y1} and S_{y2} , respectively. ϕ_{x1} , ϕ_{x2} , ϕ_{y1} and ϕ_{y2} each separately represents the magnetic flux of air-gaps S_{x1} , S_{x2} , S_{y1} and S_{y2} . When magnetic permeability P_{x1} and P_{x2} are the same, it is the zero eccentric displacement position in the x direction. Similarly, when magnetic permeability P_{y1} and P_{y2} are the same, it is the zero eccentric displacement position in the y direction.

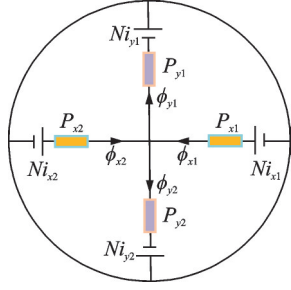


Fig.3 Equivalent magnetic circuit

From Fig.3, the flux of each air-gap can be expressed as

$$\begin{cases} \phi_{x1} = -\frac{NP_{x1}}{\sigma P} (P_{x2}(i_{x1} - i_{x2}) + P_{y1}(i_{y1} + i_{x1}) + P_{y2}(i_{x1} + i_{y2})) \\ \phi_{x2} = -\frac{NP_{x2}}{\sigma P} (P_{x1}(i_{x2} - i_{x1}) + P_{y1}(i_{y1} + i_{x2}) + P_{y2}(i_{x2} + i_{y2})) \\ \phi_{y1} = -\frac{NP_{y1}}{\sigma P} (P_{x1}(i_{x1} + i_{y1}) + P_{x2}(i_{x2} + i_{y1}) + P_{y2}(i_{y1} - i_{y2})) \\ \phi_{y2} = -\frac{NP_{y2}}{\sigma P} (P_{x1}(i_{x1} + i_{y2}) + P_{x2}(i_{x2} + i_{y2}) + P_{y1}(i_{y2} - i_{y1})) \end{cases} \quad (1)$$

where i_{x1} , i_{x2} , i_{y1} and i_{y2} are the control currents winding wound on the suspension poles S_{x1} , S_{x2} , S_{y1} and S_{y2} , respectively. σ is the leakage coefficient of permanent magnet magnetic circuit, N the number of turns of the control winding coil, and P the total permeance of the air gap, which can be defined as

$$P = P_{x1} + P_{x2} + P_{y1} + P_{y2} \quad (2)$$

In addition, the suspension force of each channel can also be obtained by Eq.(3).

$$\begin{cases} F_x = \frac{\phi_{x1}^2 - \phi_{x2}^2}{\mu_0 \beta_r l_{da} r} \\ F_y = \frac{\phi_{y1}^2 - \phi_{y2}^2}{\mu_0 \beta_r l_{da} r} \end{cases} \quad (3)$$

where F_x and F_y are the suspension forces of the X and Y channels. l_{da} is the axial length of the stator core, $\mu_0 = 4\pi \times 10^{-7}$ H/m the vacuum permeability, β_r the rotor pole arc, and r the outer radius of the rotor.

In order to obtain the accurate mathematical model of suspension force, the permeability of the air gap is calculated by the segmented magnetic

field method. During the rotation of the rotor, there are mainly two different constant force calculation cases. One is the position where only one rotor pole overlaps with the suspension pole, and the other is the position where the two rotor poles overlap with the suspension pole. Taking air gap under the suspension pole S_{x1} as an example, the rotor position can be defined as $r\theta + x_0 \leq \beta_0$ and $\beta_0 \leq r\theta + x_0 \leq \beta_0 + 0.5\beta_r$, where θ is the rotor position, x_0 the offset of the rotor in the x direction, β_{sr} the suspended pole arc, and β_0 the defined as $0.5(\beta_{sr} - \beta_r)$.

Fig.4 shows the different flux paths of the air gap under the suspension pole S_{x1} at the two rotor positions. It can be seen that the durability of the air gap changes with the change of rotor position.

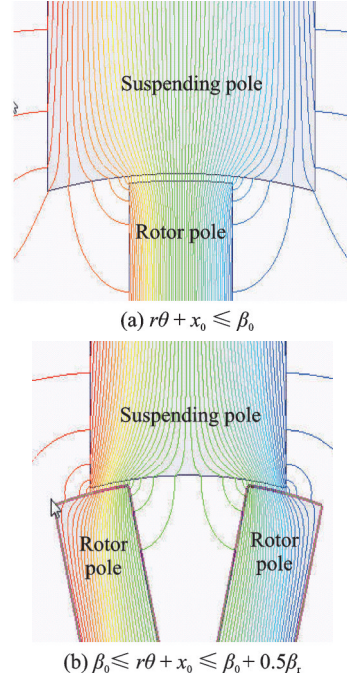


Fig.4 Magnetic flux of different rotor positions

Fig.5 shows the composition of the air gap and part of the magnetic circuit. Magnetic circuit simplification of the air gap under the suspension pole S_{x1} at different rotor positions is shown in Fig.5. As can be seen from Fig.5, the magnetic circuit of the air gap under the suspension pole S_{x1} can be expressed as two parts, where the edge flux path can be regarded as elliptical path, and the overlapping part of the rotor pole and the suspension pole can be regarded as a straight path. The position, where the cen-

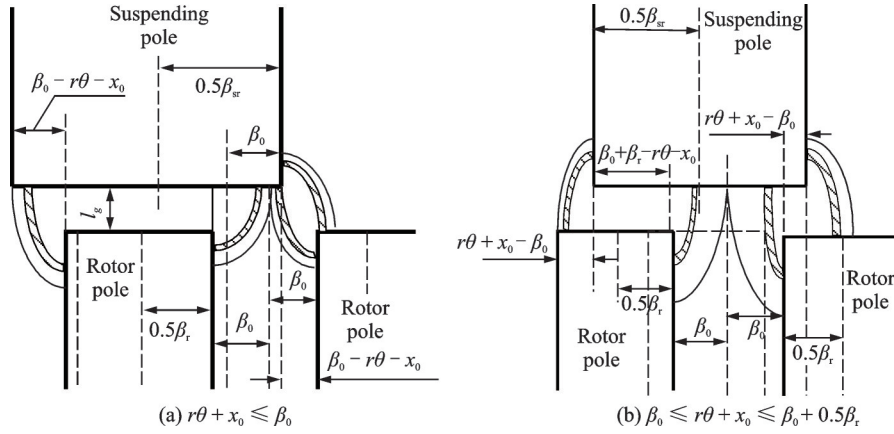


Fig.5 Composition of air-gap and some magnetic paths

terline of the suspending pole is aligned with the centerline of the rotor pole, is defined as the zero rotor position.

$$\left\{ \begin{array}{l} P_{x1} = \frac{\mu_0 l_{da} r \beta_r}{l_0 - x_0 + 0.5 y_0 \theta} + \frac{\mu_0 l_{da}}{a\pi - 2} \left(a \ln \frac{al_a + r\beta_0}{al_a} + \frac{a\pi - 4}{\pi} \ln \frac{2l_a + \pi r\beta_0}{2l_a} \right) + \\ \frac{\mu_0 l_{da}}{a\pi - 2} \left(a \ln \frac{al_a - r\theta - y_0 + r\beta_0}{al_a} + \frac{a\pi - 4}{\pi} \ln \frac{2l_a + \pi(r\beta_0 - r\theta - y_0)}{2l_a} \right) \\ P_{x2} = \frac{\mu_0 l_{da} r \beta_r}{l_0 + x_0 + 0.5 y_0 \theta} + \frac{\mu_0 l_{da}}{a\pi - 2} \left(a \ln \frac{al_a + r\beta_0}{al_a} + \frac{a\pi - 4}{\pi} \ln \frac{2l_a + \pi r\beta_0}{2l_a} \right) + \\ \frac{\mu_0 l_{da}}{a\pi - 2} \left(a \ln \frac{al_a - r\theta - y_0 + r\beta_0}{al_a} + \frac{a\pi - 4}{\pi} \ln \frac{2l_a + \pi(r\beta_0 - r\theta - y_0)}{2l_a} \right) \end{array} \right. \quad (4)$$

where $a=1.2$ is the length coefficient, the air gap elliptical major axis length $l_m = l_a + x^2/(al_a + x)$ and the fringe magnetization length $l = l_a + x\pi/2$, and x

is the total linear displacement of rotor.

In addition, the permeance of air-gap in Y channel can be expressed as

$$\left\{ \begin{array}{l} P_{y1} = \frac{\mu_0 l_{da} (r\beta_r + r\beta_0 - r\theta - x_0)}{l_0 - y_0 + 0.5 x_0 \theta} + \frac{4\mu_0 l_{da}}{\pi} \ln \frac{a\pi r^2 \theta^2 l_0 + arl_0^2 (\pi + 2) \theta + 2al_0^3 + (2\pi r\theta + (\pi + 2)l_0)(rx_0\theta - l_0 x_0)}{2a^2 l_0^3} - \\ \frac{\mu_0 l_{da}}{\pi(a\pi - 2)} \ln \frac{(a\pi r^2 \theta^2 + arl_0(\pi + 2) + 2al_0^2 + (a\pi - 2)(rx_0\theta - al_0 x_0))}{2(r\theta + al_0)^2} \\ P_{y2} = \frac{\mu_0 l_{da} (r\beta_r + r\beta_0 - r\theta - x_0)}{l_0 + y_0 + 0.5 x_0 \theta} + \frac{4\mu_0 l_{da}}{\pi} \ln \frac{a\pi r^2 \theta^2 l_0 + arl_0^2 (\pi + 2) \theta + 2al_0^3 + (2\pi r\theta + (\pi + 2)l_0)(rx_0\theta - l_0 x_0)}{2a^2 l_0^3} - \\ \frac{\mu_0 l_{da}}{\pi(a\pi - 2)} \ln \frac{(a\pi r^2 \theta^2 + arl_0(\pi + 2) + 2al_0^2 + (a\pi - 2)(rx_0\theta - al_0 x_0))}{2(r\theta + al_0)^2} \end{array} \right. \quad (5)$$

where x_0 is the eccentric displacement in the x direction, y_0 the eccentric displacement in the y direction, and l_0 the length of the air gap without eccentric displacement. l_a is defined as

$$l_a = l_0 - x_0 + \frac{y_0 \theta}{2} \quad (6)$$

When the rotor is in the position region of $\beta_0 \leq r\theta + x_0 \leq \beta_0 + 0.5\beta_r$, the permeance of each air-gaps at X channel can be obtained as

$$\left. \begin{aligned}
 P_{x1} &= \frac{\mu_0 l_{da}(r\beta_r + r\beta_0 - r\theta - y_0)}{l_0 - x_0 + 0.5y_0\theta} + \frac{4\mu_0 l_{da}}{\pi} \ln \frac{a\pi r^2(\theta - \beta_0)^2 l_0 + arl_0^2(\pi + 2)(\theta - \beta_0) + 2al_0^3 + (2\pi r(\theta - \beta_0) + (\pi + 2)l_0)(rx_0(\theta - \beta_0) - l_0 y_0)}{2a^2 l_0^3} - \\
 &\frac{\mu_0 l_{da}}{\pi(a\pi - 2)} \ln \frac{(a\pi r^2(\theta - \beta_0)^2 + arl_0(\pi + 2) + 2al_0^2 + (a\pi - 2)(ry_0(\theta - \beta_0) - al_0 y_0))}{2(r(\theta - \beta_0) + al_0)^2} \\
 P_{x2} &= \frac{\mu_0 l_{da}(r\beta_r + r\beta_0 - r\theta - y_0)}{l_0 + x_0 + 0.5y_0\theta} + \frac{4\mu_0 l_{da}}{\pi} \ln \frac{a\pi r^2(\theta - \beta_0)^2 l_0 + arl_0^2(\pi + 2)(\theta - \beta_0) + 2al_0^3 + (2\pi r(\theta - \beta_0) + (\pi + 2)l_0)(rx_0(\theta - \beta_0) - l_0 y_0)}{2a^2 l_0^3} - \\
 &\frac{\mu_0 l_{da}}{\pi(a\pi - 2)} \ln \frac{(a\pi r^2(\theta - \beta_0)^2 + arl_0(\pi + 2) + 2al_0^2 + (a\pi - 2)(rx_0(\theta - \beta_0) - al_0 y_0))}{2(r(\theta - \beta_0) + al_0)^2}
 \end{aligned} \right\} \tag{7}$$

Furthermore, the permeance of air-gaps at Y channel can be expressed as

$$\left. \begin{aligned}
 P_{y1} &= \frac{\mu_0 l_{da} r\beta_r}{l_0 - y_0 + 0.5x_0\theta} + \frac{\mu_0 l_{da}}{a\pi - 2} \left(a \ln \frac{al_a + r\beta_0}{al_a} + \frac{a\pi - 4}{\pi} \ln \frac{2l_a + \pi r\beta_0}{2l_a} \right) + \\
 &\frac{\mu_0 l_{da}}{a\pi - 2} \left(a \ln \frac{al_a - r\theta - x_0}{al_a} + \frac{a\pi - 4}{\pi} \ln \frac{2l_a - \pi(r\theta + x_0)}{2l_a} \right) \\
 P_{y2} &= \frac{\mu_0 l_{da} r\beta_r}{l_0 + y_0 + 0.5x_0\theta} + \frac{\mu_0 l_{da}}{a\pi - 2} \left(a \ln \frac{al_a + r\beta_0}{al_a} + \frac{a\pi - 4}{\pi} \ln \frac{2l_a + \pi r\beta_0}{2l_a} \right) + \\
 &\frac{\mu_0 l_{da}}{a\pi - 2} \left(a \ln \frac{al_a - r\theta - x_0}{al_a} + \frac{a\pi - 4}{\pi} \ln \frac{2l_a - \pi(r\theta - x_0)}{2l_a} \right)
 \end{aligned} \right\} \tag{8}$$

Substituting Eqs.(4—8) into Eq.(1), the levitation force can be obtained from Eq.(3). Fig.6 shows the suspension force at different control currents within one rotor pole-pitch using the mathematical model. As shown in Fig.6, the suspension force increases with the rising of the control current. The maximum error between the mathematical model and the finite element method is about 2 N. In addition, there is a small variation in the suspension force as the rotor rotates.

Since that the suspension force is a nonlinear parameter determined by the control current and ro-

tor eccentric displacement. Current stiffness and displacement stiffness are defined as the variation ratio of force to current and displacement, respectively. The current stiffness and displacement stiffness can be calculated as

$$\begin{cases} G_i = \frac{\partial F_m}{\partial i} \\ G_d = \frac{\partial F_m}{\partial s} \end{cases} \quad m = x, y \tag{9}$$

where G_i and G_d are the current stiffness and displacement stiffness, respectively, and F_m ($m=x, y$) the suspension forces generated by windings in vertical directions of x and y . i is the control current, and s the eccentric displacement value.

3 Rotor-Dynamic Modeling

This section mainly gives the rotor-dynamic model with the internal rotor structure. Making reasonable assumptions about the overall system:

- (1) Four channels of the rotor system are completely symmetrical and the parameters are the same.

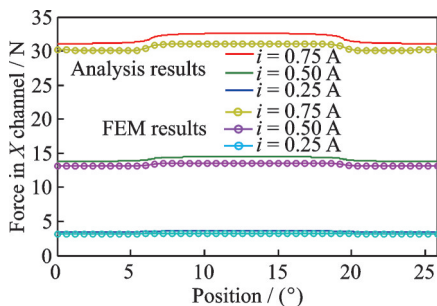


Fig.6 Levitation force with different control currents and rotor positions

(2) Allowing the rotor system to linearize in a small range at zero operating point.

(3) There is no coupling between the rotor system and the motor drive system.

Based on the conclusion of the previous section, the dynamic model of the rotor system is firstly established as

$$\begin{cases} m\ddot{x} = f_x + f_{xr} \\ J_y\ddot{\beta} - H\dot{\alpha} = p_y + p_{yr} \\ m\ddot{y} = f_y + f_{yr} \\ J_x\ddot{\alpha} + H\dot{\beta} = p_x + p_{xr} \end{cases} \quad (10)$$

where x , y are the displacements; J_x , J_y the moments of inertia; f_x and f_y the bearing forces; and f_{xr} and f_{yr} the perturbations. H is the rotor angular momentum, β the rotor radial position, α the rotor axial position, p_x the suspension moment of force in x direction, p_y the suspension moment of force in y direction, and $H=J_z\Omega$, Eq.(10) can be written as a matrix of

$$\mathbf{M}\ddot{\mathbf{q}} + \mathbf{G}\dot{\mathbf{q}} = \mathbf{f} + \mathbf{f}_i \quad (11)$$

where $\mathbf{M} = [m \ 0 \ 0 \ 0; 0 \ J_y \ 0 \ 0; 0 \ 0 \ m \ 0; 0 \ 0 \ 0 \ J_x]$, $\mathbf{G} = [0 \ 0 \ 0 \ 0; 0 \ 0 \ 0 \ H; 0 \ 0 \ 0 \ 0; 0 \ -H \ 0 \ 0]$, $\mathbf{f} = [f_x; p_y; f_y; -p_x]$, $\mathbf{f}_i = [f_{xr}; p_{yr}; f_{yr}; -p_{xr}]$, $\mathbf{q} = [x; \beta; y; -\alpha]$.

Among them, suspending forces of the X channel and the Y channel are expressed as

$$\begin{cases} f_x = k_{\text{emb}} \left[\frac{(I_0 + i_x)^2}{(\delta_0 - x)^2} - \frac{(I_0 - i_x)^2}{(\delta_0 + x)^2} \right] \\ f_y = k_{\text{emb}} \left[\frac{(I_0 + i_y)^2}{(\delta_0 - y)^2} - \frac{(I_0 - i_y)^2}{(\delta_0 + y)^2} \right] \end{cases} \quad (12)$$

where the coefficient $k_{\text{emb}} = \mu_0 N^2 A / 4$, A is the half of the cross-sectional area. x and y are the rotor displacements; and i_x and i_y the control currents. δ_0 is

the length of air-gap in rotor balance position and I_0 the bias currents. Linearize the above suspending force in a small range at the balance position, shown as

$$\begin{cases} f_x = k_h x + k_i i_x \\ f_y = k_h y + k_i i_y \end{cases} \quad (13)$$

where k_h is defined as the displacement stiffness, and k_i is defined as the current stiffness.

In the control system, each control channel consists of displacement sensor, controller and power amplifier. In order to simplify the analysis, the transfer function of controller and power amplifier can be described as $G_c(\cdot)$, therefore suspending current matrix I_i is explained as

$$I_i = G_c(Z - Q_s) \quad (14)$$

where Z is the reference input of levitation control system; and Q_s the rotor displacement vector with displacement sensor coordinate. In the control system, PID controller is adopted. Therefore, the current in the suspending winding is expressed as

$$I_i = - \left(\mathbf{K}_P q_s + \mathbf{K}_I \int q_s dt + \mathbf{K}_D \dot{q}_s \right) \quad (15)$$

where \mathbf{K}_P , \mathbf{K}_I , \mathbf{K}_D are the proportional coefficient matrix, the integral coefficient matrix and the differential coefficient matrix, respectively. q_s is the displacement.

Based on suspending force and rotor dynamics, the control scheme of the proposed BLSRM is shown in Fig.7. In Fig.7, $(x_{\text{ref}}, y_{\text{ref}})$ and $i_{x,y,\text{ref}}$ are the reference displacement and current; $e_{x,y}$ and $e_{ix,y}$ the deviations between reference and true value; $u_{x,y}$, $i_{x,y}$, $F_{x,y}$ and (x,y) the actual voltage, current, axial force and displacement in vertical directions; $k_{i(x,y)}$ and $k_{x(x,y)}$ the current and the displacement stiffness, and L and R the inductance and reluctance of sus-

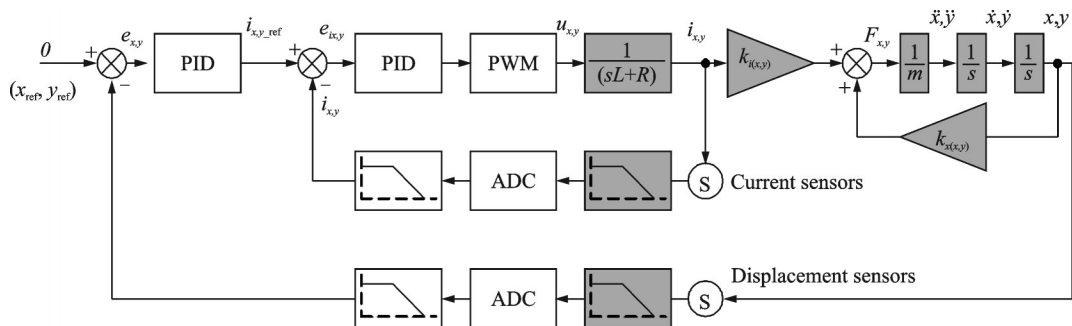


Fig.7 Control scheme of the proposed BLSRM

pension winding. PID is the proportion-integration-differentiation controller, PWM the pulse width modulation switching driver and ADC is the analog to digital converter.

4 Experimental Verification

4.1 Experimental platform

To test the suspension performance of the proposed BLSRM, one prototype motor is manufactured, as shown in Fig.8. Fig.8 shows the experimental platform, including the controller, motor, oscilloscope, and power supply. The motor parameters are shown in Table 1.

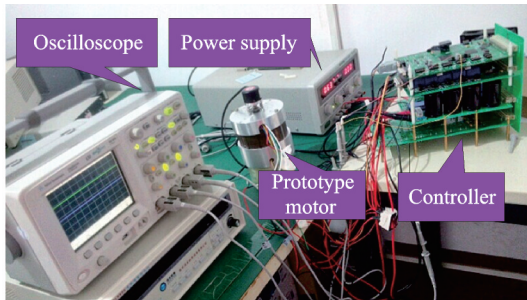


Fig.8 Experimental platform and prototype motor

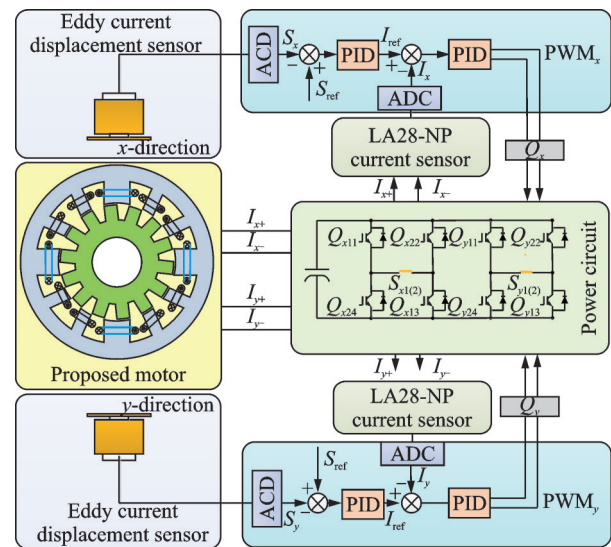
Table 1 Prototype parameters

Parameter	Value
Number of stator poles	12
Number of rotor poles	14
Torque pole arc/ (°)	10
Radial force pole arc/ (°)	25.7
Rotor pole arc/ (°)	13
Axial stacking length/mm	40
Stator outer diameter/mm	112
Rotor outer diameter/mm	58
Rotor inner diameter/mm	20
Number of turns of the suspension bias pole winding	200
Number of turns of the torque pole winding	180
Rotor mass/kg	0.234
Rated power/W	200
Rated speed/ (r·min ⁻¹)	10 000
Rated voltage/V	300

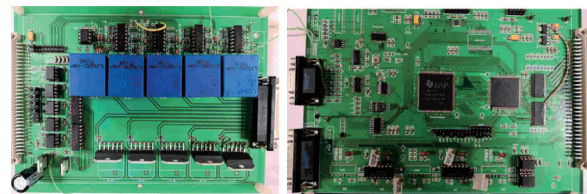
4.2 Implementation of PID controller for rotor system

According to the principle of BLSRM suspension system, motor suspension is related to the differential flux. In suspension control, the motor sus-

pension is controlled by driving PWM signal to change the size of the control current. Therefore, suspension system mainly includes displacement sensor, digital signal processor, driving circuit, power circuit and so on. Digital signal processor is TMS320F28335, in which the main frequency of 150 MHz. The driving circuit is composed of optical coupling isolation circuit and switching power amplifier circuit. The power circuit adopts DC-DC module. The experimental schematic diagram of rotor suspension system is shown in Fig.9. In Fig.9, S_{ref} and I_{ref} are the displacement and the current reference, and S_x , S_y , I_x and I_y the actual displacement and the current in vertical directions of x and y . $PWM_{x,y}$ represents the duty circle commands and $Q_{x,y}$ the transistor selection sequence.



(a) Schematic diagram



(b) Power circuit

Fig.9 Suspension control system

Each suspension channel in the suspension system is independently controlled by one PWM signal and one driver signal. Firstly, the measured rotor displacement and coil current are input to the processor through the conditioning circuit and A/D conversion. Based on the PID control law, the PWM duty

ratio required for suspension is calculated by the processor. The switching signal with certain driving ability is generated through the opto-coupling isolation circuit. Accordingly, current in suspension winding can be controlled to produce suspension force.

4.3 Static experiments

Fig.10 shows the control currents of the four control windings in the static state, where all torque windings are turned off. Once the control current is given, the control current increases and the appropriate control current is reached within short time.

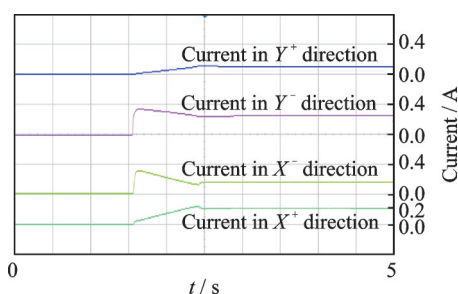


Fig.10 Currents in four control windings under static condition

Fig.11 shows the rotor eccentric displacement and current in the X channel static state. The displacement of the X channel given command is set to zero to keep the rotor position in the center. It can be seen that in the X channel stationary state, the rotor moves to the equilibrium position when applying the bearingless controller. In addition, the control current of the suspending winding is less than 0.4 A.

Fig.12 shows the experimental results when one external force suddenly acts on the rotor. Once

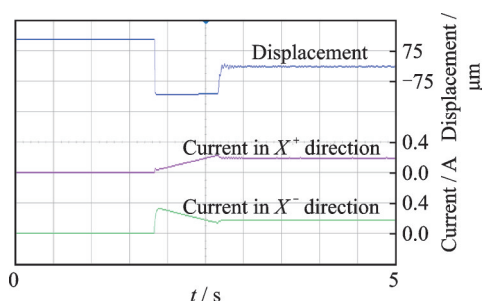


Fig.11 Eccentric displacement and current under static condition of X channel

the rotor is perturbed, the rotor eccentric displacement and control current change instantaneously, rotor also moves to balance position. From the results it can be seen that the control current changes over a period of time and the adjustment time is less than 0.3 s.

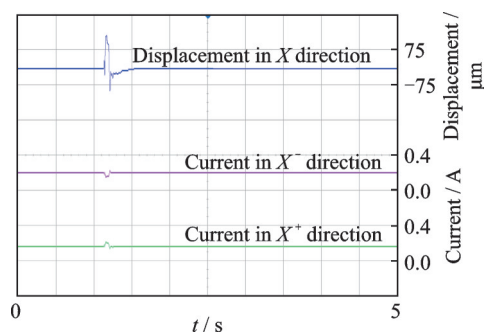


Fig.12 Eccentric displacement and current with external force disturbance

4.4 Rotational experimentation

Fig.13 shows the rotor eccentric displacement with two degrees of freedom and the torque current of the two torque windings. The motor speed command is set to 2 000 r/min. The maximum eccentric displacement is less than 75 μm . The results show that the rotor can be stably controlled in the equilibrium position and obtain effective suspension performance.

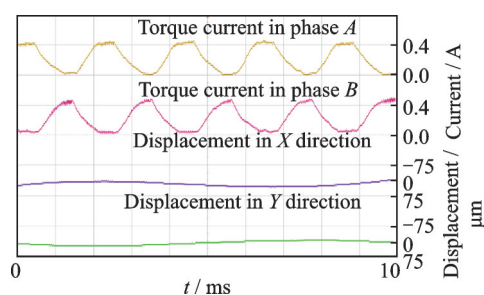


Fig.13 Rotor displacement and torque current at 2 000 r/min

The levitation force is measured using the experimental platform, and the test results are shown in Fig.14. The experimental results are similar to that of the analysis result and the FEM result, with maximum errors of 0.73 N and 1.28 N, respectively. In addition, the linear relationship between the suspension force and the control current assure better control performance.

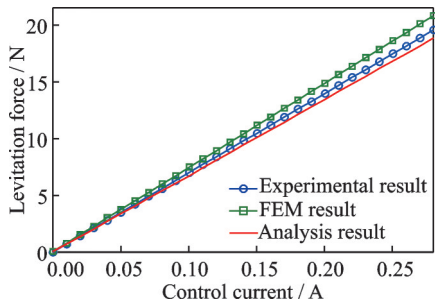


Fig.14 Test result of levitation force

Table 2 shows the current and displacement stiffness of the rotor in the center position. Compared to the mathematical model (analysis) and finite element analysis, the maximum error of the experimental results for levitation force is 3.87%, for current stiffness is 3.33%, and for displacement stiffness is 0.94%.

Table 2 Current stiffness and displacement stiffness

Index	Experiment	Analysis	FEM
Levitation force/ N	19.60	18.87	20.88
Current stiffness/(N•A ⁻¹)	69.75	67.39	67.50
Displacement stiffness/(N•mm ⁻¹)	-227.84	-230.01	-231.63

5 Conclusions

One control scheme for rotor displacement of 12/14 structure BLSRM is presented and analyzed. From the static and dynamic experimental results, the BLSRM motor can be steadily suspended at the balanced position. Through theoretical analysis, finite element simulation and experimental verification, the error of the suspended force is very small, and the linear relationship between the suspension force and the control current also assure better control performance.

References

[1] CAO Xin, CHEN Huateng, DENG Zhiqian. Analogy study of two types of multi-degree-of-freedom switched reluctance motors[J]. Journal of Nanjing University of Aeronautics & Astronautics, 2020, 52(2): 171-180.(in Chinese)

[2] HAO Zhenyang, MIAO Wei, CAO Xin, et al. Two

different role division control strategies for torque and axial force of conical bearingless switched reluctance motor[J]. Transactions of Nanjing University of Aeronautics and Astronautics, 2020, 37(6): 848-857.

[3] ZHANG Tao, CHEN Jie, ZHU Weiguo. Suspension performance analysis on the novel hybrid stator type bearingless switched reluctance motor[J]. IEEE Transactions on Magnetics, 2021, 57(6): 1-4.

[4] YANG Yan, ZHU Weiming, LIU Zeyuan, et al. Vibration and noise reduction of bearingless switched reluctance motor based on shape optimization method[J]. Journal of Nanjing University of Aeronautics & Astronautics, 2022, 54(2): 332-340.(in Chinese)

[5] WANG Huijun, BAO Junfang, XUE Bingkun, et al. Control of suspending force in novel permanent-magnet-biased bearingless switched reluctance motor[J]. IEEE Transactions on Industrial Electronics, 2015, 62(7): 4298-4306.

[6] YANG Yan, DENG Zhiqian, YANG Gang, et al. A control strategy for bearingless switched-reluctance motors[J]. IEEE Transactions on Power Electronics, 2010, 25(11): 2807-2819.

[7] CUI Ruizhen, WANG Xilian, HUANG Zhuliang, et al. Minimum energy consumption control strategy of bearingless switched reluctance motor with sharing suspension windings[J]. Proceedings of the CSEE, 2023, 43(13): 5229-5239.

[8] ZHU Tao, CAO Xin, YU Qiang, et al. Direct torque control with phase commutation optimization for single-winding bearingless switched reluctance motor[J]. IEEE Transactions on Power Electronics, 2022, 37(11): 13238-13249.

[9] CHEN Li, HOFMANN W. Speed regulation technique of one bearingless 8/6 switched reluctance motor with simpler single winding structure[J]. IEEE Transactions on Industrial Electronics, 2012, 59(6): 2592-2600.

[10] ZHOU Heng, CAO Xin, QIAO Yanchen, et al. A novel 6/4 conical bearingless switched reluctance motor[C]//Proceedings of the 2015 18th International Conference on Electrical Machines and Systems (ICEMS). Pattaya City, Thailand: IEEE, 2015.

[11] WANG Zelin, CAO Xin, DENG Zhiqian, et al. Modeling and characteristic investigation of axial reluctance force for bearingless switched reluctance motor[J]. IEEE Transactions on Industry Applications, 2021, 57(5): 5215-5226.

- [12] HAO Zhenyang, CAO Xin, DENG Xu, et al. Novel bearingless switched reluctance motor with wide flat inductance region to simplify the control of torque and levitation force[J]. *IEEE Transactions on Energy Conversion*, 2020, 35(3): 1278-1288.
- [13] LEE D H, WANG HUIJUN, AHN J W. Modeling and control of novel bearingless switched reluctance motor[C]//*Proceedings of the 2009 IEEE Energy Conversion Congress and Exposition*. San Jose, CA, USA: IEEE, 2009.
- [14] XU Zhenyao, LEE D H, AHN J W. Comparative analysis of bearingless switched reluctance motors with decoupled suspending force control[J]. *IEEE Transactions on Industry Applications*, 2015, 51(1): 733-743.
- [15] YUE Qi, XU Zhenyao, YUE Zhang. Characteristics analysis of a novel hybrid rotor type 12/14 bearingless switched reluctance motor[C]//*Proceedings of the 2021 24th International Conference on Electrical Machines and Systems (ICEMS)*. Hybrid, Korea: IEEE, 2021.
- [16] WANG Huijun, LIU Jianfeng, BAO Junfang, et al. A novel bearingless switched reluctance motor with a biased permanent magnet[J]. *IEEE Transactions on Industrial Electronics*, 2014, 61(12): 6947-6955.
- [17] WANG Huijun, LI Fangxun. Design consideration and characteristic investigation of modular permanent magnet bearingless switched reluctance motor[J]. *IEEE Transactions on Industrial Electronics*, 2020, 67(6): 4326-4337.
- [18] ASAMA J, KANEHARA D, OIWA T, et al. Suspension performance of a two-axis actively regulated consequent-pole bearingless motor[J]. *IEEE Transactions on Energy Conversion*, 2013, 28(4): 894-901.
- [19] ZHANG Tao, CHEN Jie, ZHU Weiguo. Suspension performance analysis on the novel hybrid stator type bearingless switched reluctance motor[J]. *IEEE Transactions on Magnetics*, 2021, 57(6): 1-4.
- [20] WANG Zelin, CAO Xin, DENG Zhiqian, et al. High integrated methodology and evaluation for switched-reluctance type bearingless motors with five degree of freedom magnetic levitation[J]. *IEEE Transactions on Energy Conversion*, 2023, 38(2): 759-770.
- [21] YANG Fan, YUAN Ye, SUN Yukun, et al. Coupling suspension force regulator considering time-varying characteristic for a bearingless switched reluctance motor[J]. *IEEE Transactions on Industrial Electronics*, 2023, 70(7): 6632-6641.
- [22] XUE Bingkun, WANG Huijun, TANG Shaofei. Stiffness analysis for bearingless switched reluctance motor with bias permanent magnet[C]//*Proceedings of the 2015 IEEE International Magnetics Conference (INTERMAG)*. Beijing, China: IEEE, 2015.

Authors Mr. WANG Chuanchuan received the B.S. degree in detection, guidance, and control technology from Central South University, Changsha, China, in 2020, and received the M.S. degree in instrumentation and optoelectronic engineering from Beihang University, Beijing, China, in 2022. His research interests are rotor displacement self-sensing methods and sensor-less control of Bearingless switched reluctance motor.

Prof. WANG Huijun received the M.S. degree in electrical engineering from Shenyang University of Technology, Shenyang, China, in 2003 and the Ph.D. degree in electrical and mechatronics engineering from Kyungshung University, Busan, South Korea, in 2009. He is currently with the School of Instrumentation Science and Optoelectronics Engineering, Beihang University, Beijing, China. His research interest includes motor design and drive system.

Author contributions Mr. WANG Chuanchuan designed the overall content of the research, established the theoretical model, conducted the derivation and analysis, then analyzed the experimental results and wrote the the manuscript. Prof. WANG Huijun improved and refined the research approach and revised the logical structure of the manuscript. Mr. ZHANG Junhao designed the experimental setup and conducted the experiments. Ms. JIN Lu contributed to model derivation and guided the manuscript writing. Ms. NIU Zhaoxiang enhanced and optimized the model. Mr. DU Juncheng provided technical support for the experiments. All authors commented on the manuscript draft and approved the submission.

Competing interests The authors declare no competing interests.

(Production Editor: SUN Jing)

一种定子单绕组无轴承开关磁阻电机的转子位移控制方法

王川川¹, 张峻豪¹, 金璐², 牛赵翔¹, 杜军成¹, 王惠军¹

(1. 北京航空航天大学仪器科学与光电工程学院, 北京 100191, 中国;

2. 浙江西子富沃德电机有限公司, 杭州 311300, 中国)

摘要:提出了一种用于定子单绕组无轴承开关磁阻电机(Bearingless switched reluctance motor, BLSRM)的转子位移控制方法。首先介绍了定子单绕组无轴承开关磁阻电机的基本结构和工作原理,基于等效磁路法建立悬浮力和刚度的数学模型。其次,建立了转子动力学模型以获取悬浮力与转子位移间的关系模型。最后,设计了一台实验样机并在电机上进行悬浮控制实验。实验结果验证了所提控制方法的有效性。

关键词:无轴承开关磁阻电机;转子位移;单绕组定子;控制